Journal of Nuclear Materials 427 (2012) 152–161

Contents lists available at SciVerse ScienceDirect

Journal of Nuclear Materials

journal homepage: www.elsevier.com/locate/jnucmat

Simulation of irradiation induced deuterium trapping in tungsten

T. Ahlgren *, K. Heinola, K. Vörtler, J. Keinonen

Accelerator Laboratory, University of Helsinki, P.O. Box 43, 00014 Helsinki, Finland

ARTICLE INFO

Article history:
Received 4 April 2012
Accepted 25 April 2012
Available online 3 May 2012

ABSTRACT

Particle irradiation produces defects which trap hydrogen isotopes and impurities in nuclear reactor materials. However, a comprehensive understanding of the basic mechanisms, and the final outcome of this process is still lacking. Here the evolution of defects, hydrogen, and impurities in tungsten during and after deuterium irradiation is simulated by solving rate theory equations. The results are in excellent agreement with irradiation experiments. Our results show that hydrogen is mainly trapped in tungsten monovacancies, and trapping in larger vacancy clusters increase with increasing implantation energy. The slow hydrogen desorption observed in experiments after irradiation, was found to be mainly due to detrapping of the weakly bound sixth hydrogen from monovacancies. Impurities are shown to play a significant role in decreasing Frenkel pair annihilation during irradiation, by trapping self-interstitial atoms. Moreover, we conclude that the formed impurity self-interstitial atom complexes could be the nucleation site for formation of large interstitial type dislocation loops observed experimentally.

© 2012 Elsevier B.V. All rights reserved.

1. Introduction

The refractory metal tungsten (W) has extraordinary physical and thermal properties. Among other reasons why W is intended to be used as a plasma facing component in the next step fusion device ITER [1,2], is that it has a high energy threshold for physical sputtering and does not normally form hydrides. As a first wall material in ITER, W will be subjected to both low energy, high flux hydrogen (H) isotopes, and high energy neutrons that will create H trapping damage deep in the wall material. The H isotope retention should be kept as low as possible for both fusion efficiency and safety reasons. The natural and irradiation-induced traps will retain H isotopes and especially important is the tritium (T) retention.

There are many studies where hydrogen irradiation and trapping in W have been modeled [3–8]. The main difficulty in these simulations lies in that the irradiation is a dynamic process, where the creation, migration and evolution of defects, impurities and H all have to be taken into account. To our knowledge, the presently used modeling codes relying on the rate theory [9–11,7,12], are unable to take into account these dynamic defect evolution processes during irradiation. This means that the simulations are usually started after the irradiation part, focussing on the H detrapping and thermal desorption portion of the experiments. Obvious complications following this scheme are that the initial H trap concentrations have to be chosen somehow, and that the possible thermal evolution of the traps are not accounted for.

In the present work, instead of bypassing the above-mentioned obstacle, the dynamic processes during irradiation have been included in the simulation code.

Another simulation method fulfilling the required time and depth scales is the Kinetic Monte Carlo (KMC) method. In KMC simulations the time step is inversely proportional to the sum of frequencies for all processes. If the system involves an extremely fast moving object, like the self-interstitial atom (SIA) in W [13–15], the KMC time step at room temperature is of the order of 10^{-11} s. Clearly, long simulation times and high defect concentrations are inaccessible with KMC.

The purpose of the present work is to understand H trapping and defect evolution in bcc metals, and especially in W, by extending the rate theory models, to include also all dynamic processes during the irradiation.

The simulation method and parameters are introduced in Section 3. The simulations are validated by comparison with the experimental results in Section 4, and the results are used to elucidate some important experimental data reported in the literature.

2. Experimental

The simulations are compared to experimental results on implantation of deuterium (D) into polycrystalline W at room temperature, to a fluence of 5.8×10^{20} D/m^2, with three different implantation energies, 5, 15 and 30 keV/D. The flux was about 3.2×10^{17} D/m^2 s. The main impurity, excluding Mo, in the W samples was carbon (C) $\sim$ 10 µg/g, corresponding to about 10^{25} C atoms/m^3 (typical high purity 99.99% polycrystalline W by Plansee AG). The experimental details are described elsewhere [16].

* Corresponding author.
E-mail address: tommy.ahlgren@helsinki.fi (T. Ahlgren).

0022-3115/$ - see front matter © 2012 Elsevier B.V. All rights reserved.
http://dx.doi.org/10.1016/j.jnucmat.2012.04.031

3. Computational formalism

The simulation method presented, solves chemical rate equations (RE), where the concentration C for each examined distinct entity as a function of depth and time, is given by the following coupled partial differential equations [17–19]

$$\frac{\partial C_\alpha(x,t)}{\partial t} = D_\alpha \frac{\partial^2 C_\alpha(x,t)}{\partial x^2} + S_\alpha(x,t) \pm \sum_{\beta,\gamma=1}^{N} k^2_{\beta,\gamma} D_\beta C_\beta(x,t) \pm \sum_{\delta=1}^{N} \nu_\delta e^{-\frac{E_{A,\delta}}{kT}} C_\delta(x,t) \quad (1)$$

where α, β, γ, and δ stands for H, vacancy, SIA, impurities, and combinations of all of them. Totally there are N distinct entities. The first term on the right-hand side describes diffusion of entity α with diffusion coefficient D_α (Section 3.1).

The second term is the source term, which includes irradiation and the resulting induced defects. This term will be considered in Section 3.2.

The third term comprises all exothermic reactions described with sink strength $k^2_{\beta,\gamma}$ (Section 3.3) [20–22].

The last term in Eq. (1) is endothermic, and in general describes the reverse process of the previous term (Section 3.4). This term includes detrapping of H from vacancies, SIA, grain boundaries, dislocations and impurities, and dissociation of vacancy and SIA clusters. The ν_δ is the pre-exponential factor for detrapping or dissociation, which includes the attempt frequency and geometrical factors, and $E_{A,\delta}$ is the minimum activation energy barrier the system has to pass when the complex δ breaks up [23–26]. The choice of plus and minus sign depends on the reaction.

Using a non-uniform depth grid in the RE simulations, makes it possible to manage a nanometer dense grid close to surface, with increasing distance between grid points to cover centimeter scale lengths. The surface boundary condition for diffusing entities, was chosen so that the first bulk concentration under the surface is always zero. This is a good approximation for H in W because the energy for a system, with an H atom on the surface, is about 2 eV lower, compared to the case where the H atom is in the solute site in the bulk [27]. The numerical method for solving Eq. (1) is given in Ref. [28].

Table 1 summarizes all processes the current model can handle. The black and gray arrows indicate the diffusion and the process

Table 1
Possible events including hydrogen isotopes (H, D or T), vacancy (V), SIA (I), grain boundary (G), dislocation (ρ), surface (S), and impurities (Imp). m, n, i, and j are indexes. (For interpretation of the references to color in this figure legend, the reader is referred to the web version of this article.)

H	+	V_mH_{n-1}	⇔	V_mH_n	$1 \le m \le 5$, $0 \le n \le 6m$
H	+	I_mH_{n-1}	⇔	I_mH_n	$1 \le m \le 10$, $0 \le n \le m$
I_m	+	I_iH_j	⇒	$I_{m+i}H_j$	$m+i \le 10$, $j \le m+i$
I_m	+	V_iH_j	⇒	j H; $V_{i-m}H_j$; $I_{m-i}H_j$	$m = i$; $m < i$; $m > i$
V	+	V_mH_n	⇒	$V_{m+1}H_n$	$1 \le m \le 4$, $0 \le n \le 6m$
H	+	ρ	⇔	ρ–H	Trapping in dislocation
H	+	G	⇔	G-H	Trapping in grain boundary
H	+	Imp	⇔	Imp-H	Impurity
H	+	S	⇔	S, H	Surface
Events not including hydrogen					
V	+	V_m	⇔	V_{m+1}	$1 \le m \le 39$
V_m	+	V_n	⇒	V_{m+n}	$m+n \le 40$
I	+	I_m	⇔	I_{m+1}	$1 \le m \le 39$
I_m	+	I_n	⇒	I_{m+n}	$m+n \le 40$
I_m	+	V_n	⇒	Ø; V_{n-m}; I_{m-n}	$m = n$; $m < n$; $m > n$
V	+	ρ	⇒	ρ	Dislocation sink
V	+	G	⇒	G	Grain boundary sink
V	+	Imp	⇔	Imp-V	Impurity
V	+	S	⇒	S	Surface
I_m	+	ρ	⇒	ρ	Dislocation sink
I_m	+	G	⇒	G	Grain boundary sink
I	+	Imp	⇔	Imp-I	Impurity
I_m	+	Imp-I_n	⇔	Imp-I_{m+n}	Impurity
I_m	+	S	⇒	S	Surface

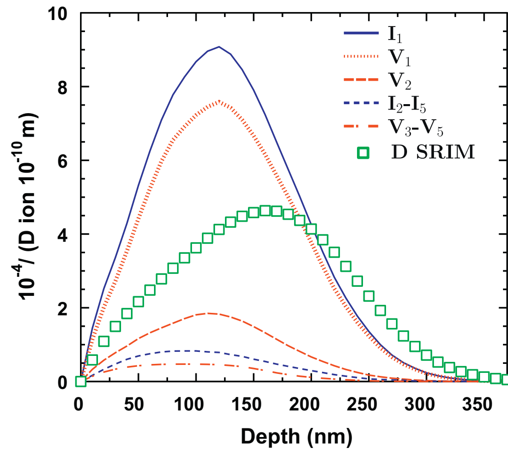

Fig. 1. Resulting D and defect profiles per incoming 30 keV D in W, obtained by SRIM and MD simulations. The profiles have been multiplied by the number of defects in each cluster, to make the larger clusters more visible. For example, the $V_3 - V_5$ profile is the sum of profiles: $3V_3 + 4V_4 + 5V_5$.

direction, respectively. The maximum cluster size for vacancies, SIAs and impurity-SIA clusters is forty defects.

Recent electron density functional theory (DFT) calculations show that a monovacancy in W can contain up to six hydrogen atoms near room temperature [15]. The maximum number of hydrogen atoms in a vacancy cluster with m vacancies is therefore equal to 6 m. The number of hydrogen atoms per SIA in a cluster was chosen to be one [15].

In summary, there are 314 distinct entities (N) that can take part in totally 3176 exothermic and 301 endothermic reactions. For simulating the experimental conditions, described in Section 2, the total RE simulation time was 24 h including 0.5 h for the processes during the implantation. The simulation depth grid covered the whole 1 mm thick W sample, with 1 nm grid point distance close to the sample surface.

3.1. Diffusion parameters

The diffusion not only spreads the concentrations profiles, but the reaction rate for any defect or impurity is proportional to its diffusion coefficient and concentration, i.e. the third term in Eq. (1). The entities that diffuse are impurities, D, monovacancies, vacancy clusters, SIAs, and SIA clusters. The diffusivity for C, the most abundant impurity in the sample, at room temperature is very small due to the large migration barrier of about 1.5 eV [29]. The migration barrier used for D was 0.26 eV, and the pre-exponential factor was taken as the H pre-exponential factor, scaled with the isotope effect $D_0^{\rm D} = D_0^{\rm H}/\sqrt{2}$ [27]. The diffusion coefficient for monovacancies at room temperature is effectively zero, due to the large migration barrier of about 1.8 eV [30]. Thus, all reactions in Table 1, involving mobile vacancies, are negligible in the present simulations.

The SIA configuration in W is the ⟨1 1 1⟩ crowdion [14], which has a very small migration barrier in the ⟨1 1 1⟩ direction [13,27]. The reorientation frequency for the SIA to change the one-dimensional (1-D) diffusion direction (rotate) is [31]

$$\Gamma_R = \nu_R e^{-E_R/kT} \tag{2}$$

where $\nu_R \approx 6.59 \times 10^{12}\,{\rm s}^{-1}$ is the pre-exponential factor, and $E_R \approx 0.385$ eV the energy barrier for rotation, respectively [13].

The diffusion coefficients for the SIA clusters are approximated as the one for a SIA, divided by the square root of cluster size as suggested by Osetsky et al. [32]. The rotation barrier was seen to increase with the SIA cluster size in molecular dynamics (MDs) simulations in bcc Fe [33]. The SIA clusters were thus assumed to diffuse with zero reorientation frequency. We tested this assumption, and no noticeable difference in the RE simulations was observed, if the SIA clusters were allowed to reorientate.

3.2. Source term

One of the most essential input parameters for the RE simulations, are the source profiles of impurities and different defect types during irradiation. These were obtained by calculating statistically accurate, implantation induced defect profiles per incoming D ($\rm m^{-1}ion^{-1}$), see Fig. 1. The profiles were then multiplied by the D flux ($\rm m^{-2}\,s^{-1}$), to give the source profile S_α ($\rm m^{-3}\,s^{-1}$). The primary D–W collision statistics were determined by SRIM [34], and the W collision cascades by MD [35], with the potential parameters from Ref. [36].

3.3. Sink strengths

Sink strengths describe how fast an impurity or defect is trapped or annihilated. Each sink type has an own sink strength, which depend on the sink size, geometry and concentration. Here three types of sink strengths are considered: (1) spherical sinks (point defects and clusters), (2) line sinks (edge dislocations), and (3) planar sinks (grain boundaries). A short introduction to how sink strengths are determined, the time dependence for the sink strength, and the sink strength for edge dislocations, including defect-dislocation interaction, is presented in Appendix A.

The sink strength for spherical absorbers, with concentration $C_\gamma(x, t)$, for three-dimensionally (3-D) migrating entities (β), is given by the following recursive expression [37,38]

$$k^2_{\beta,\gamma} = k^2_{\text{3-D}} = 4\pi R_{\beta,\gamma} C_\gamma(x,t)(1 + R_{\beta,\gamma} k_{tot}) \tag{3}$$

where $k^2_{tot} = \sum k^2_\beta$ is the sum sink strength for entity β which includes $k^2_{\beta,\gamma}$, and $R_{\beta,\gamma}$ is the reaction radius between the sink and the entity. If the distance between the sink and entity is less than this radius, the entity is trapped or absorbed by the sink. For 1-D diffusing entities (β), the sink strength for spherical absorbers becomes [39]

$$k^2_{\beta,\gamma} = k^2_{\text{1-D}} = 6\left[\pi R^2_{\beta,\gamma} C_\gamma(x,t)\right]^2 \tag{4}$$

where the term 6 (=3 × 2) includes the convention of using the equivalent 3-D diffusion coefficient in the third term in Eq. (1), i.e. $D_{\text{1-D}} = 3D_{\text{3-D}}$. In the case where the entity follows neither 1-D nor 3-D migration, the sink strength can be given as a function of the mean length before change of the diffusion direction l_{ch} as [40]

$$k^2_{\beta,\gamma} = k^2_{\text{1-3D}} = \frac{k^2_{\text{1-D}}}{2}\left(1 + \sqrt{1 + \frac{4}{x^2}}\right) \tag{5}$$

with the dimensionless variable

$$x^2 = \frac{l^2_{ch} k^2_{\text{1-D}}}{12} + \frac{k^4_{\text{1-D}}}{k^4_{\text{3-D}}}. \tag{6}$$

The sink strength for spherical grain boundary, with radius R_g is given by [37]

$$k^2_{\beta,\gamma} = \frac{1}{R_g^2}\frac{(k_{tot}R_g \coth(k_{tot}R_g) - 1)}{\left[\frac{1}{3} - \frac{\coth(k_{tot}R_g)}{k_{tot}R_g} + \frac{1}{k^2_{tot}R^2_g}\right]}. \tag{7}$$

Parameters to determine the sink strengths include, dislocation densities, mean grain boundary radius, and different reaction radii (trapping or annihilation). The W SIA-monovacancy recombination

Table 2
Parameters for the simulation of the W system at room temperature. D is deuterium, I_1 SIA, V_1 monovacancy, I_m (V_m) size m SIA (V) cluster, I_mD_n (V_mD_n) size m SIA (V) cluster with n D, Grain (G), dislocation (ρ), carbon (C), and oxygen (O). a_0=0.3165 nm is lattice constant. $\Omega = a_0^3/2$ is atomic volume. $R_\Omega = \left(\frac{3\Omega}{4\pi}\right)^{1/3}$.

Entity	Diffusion coeff. (m^2/s)		Rotation energy (eV)		Rotation pre-factor (1/s)		Ref.	Additional information
Diffusion parameters								
D	1.5×10^{-12}						[27]	$4.8 \times 10^{-8} 2^{-0.5} e^{-0.26\ \mathrm{eV/kT}}$ m^2/s
I_1	5.0×10^{-10}		0.385		6.59×10^{12}		[13]	See text in Section 3.1
I_m	$5.0 \times 10^{-10}/m^s$				0.0		[32]	$2 \leqslant m \leqslant 10$, s = 0.5, Section 3.1
Reaction radius $R_{\beta,\gamma}$ (nm)								
Annihilation, trapping and clustering parameters								
Annihilation								
I_m	+	V_n			$0.81 + R_\Omega[(m+n)^{1/3} - 2^{1/3}]$		[a]	$1 \leqslant m \leqslant 40$ and $1 \leqslant n \leqslant 40$
Trapping								
I_m	+	G, ρ	→	G, ρ				$1 \leqslant m \leqslant 10$
D	+	V_mD_{n-1}	→	V_mD_n	$0.59 + R_\Omega(m^{1/3} - 1)$		[b]	$1 \leqslant m \leqslant 5$ and $1 \leqslant n \leqslant 6$ m
D	+	I_mD_{n-1}	→	I_mD_n	$0.81 + R_\Omega(m^{1/3} - 1)$		[c]	$1 \leqslant m \leqslant 20$ and $1 \leqslant n \leqslant m$
D	+	G	→	G–D				
D	+	ρ	→	ρ–D				
D	+	O	→	O–D	0.274			Nearest neighbor dist. $\sqrt{3}a_0/2$
I_1	+	C	→	C–I_1	0.81		[c]	
Clustering								
I_m	+	I_nD_i	→	$I_{m+n}D_i$	$0.81 + R_\Omega[(m+n)^{1/3} - 2^{1/3}]$		[c]	$2 \leqslant (m+n) \leqslant 20$
I_m	+	C–I_n	→	C–I_{m+n}	$0.81 + R_\Omega[(m+n)^{1/3} - 2^{1/3}]$		[c]	$2 \leqslant (m+n) \leqslant 40$
					Attempt freq. (THz)	Activation energy $E_{A,\delta}$ (eV)		
Detrapping parameters								
V_mD_n	→	V_mD_{n-1}	+	D	12.8	1.56	[15]	$1 \leqslant m \leqslant 5$ and $1 \leqslant n \leqslant$ m
V_mD_n	→	V_mD_{n-1}	+	D	12.0	1.54	[15]	$1 \leqslant m \leqslant 5$ and $m+1 \leqslant n \leqslant 2m$
V_mD_n	→	V_mD_{n-1}	+	D	19.4	1.37	[15]	$1 \leqslant m \leqslant 5$ and $2m+1 \leqslant n \leqslant 3m$
V_mD_n	→	V_mD_{n-1}	+	D	22.0	1.26	[15]	$1 \leqslant m \leqslant 5$ and $3m+1 \leqslant n \leqslant 4m$
V_mD_n	→	V_mD_{n-1}	+	D	22.6	1.16	[15]	$1 \leqslant m \leqslant 5$ and $4m+1 \leqslant n \leqslant 5m$
V_mD_n	→	V_mD_{n-1}	+	D	26.7	0.61	[15]	$1 \leqslant m \leqslant 5$ and $5m+1 \leqslant n \leqslant 6m$
I_mD_n	→	I_mD_{n-1}	+	D	28.0	0.4–1.0	[15]	$1 \leqslant m \leqslant 20$ and $1 \leqslant n \leqslant m$
G–D	→	G	+	D	28.0	1.06	[42]	
O–D	→	O	+	D	28.0	0–1.4		No data available
C–I_m	→	C	+	I_m	5.0	0–1.4		No data available
C–I_m	→	C–I_{m-1}	+	I_1	5.0	2.12	[43]	I_2 Binding energy

[a] Annihilation radius from molecular statics, Section 3.3.
[b] From molecular statics, Section 3.3.
[c] Approx. to be same as for I–V annihilation.

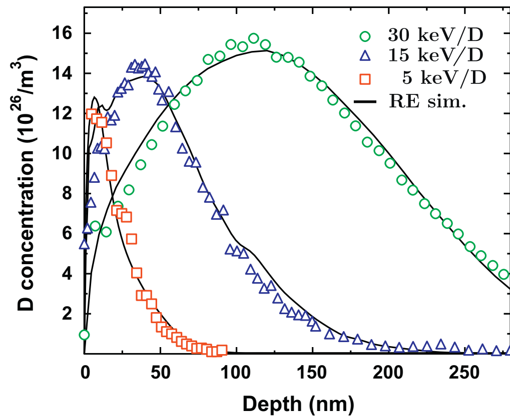

Fig. 2. Experimental and simulated D distributions in W, with implantation energies of 5, 15, and 30 keV/D, to a fluence of 5.8×10^{20} D/m^2.

radius is an ellipsoid around the SIA center, with semiminor and semimajor axis of 0.54 and 1.8 nm, respectively [36]. The spherical annihilation radius of 0.81 nm (2.6a_0, a_0 is the lattice constant in W), gives the same volume around the SIA as the volume of the ellipsoid. This rather large annihilation radius is understandable due to the wide extent of the SIA ⟨1 1 1⟩ crowdion, where about four atoms are displaced along the ⟨1 1 1⟩ direction on both sides of the central SIA atom [13,14]. The distance between the last atom in the crowdion row to the SIA center, is about 0.96 nm (≈3a_0).

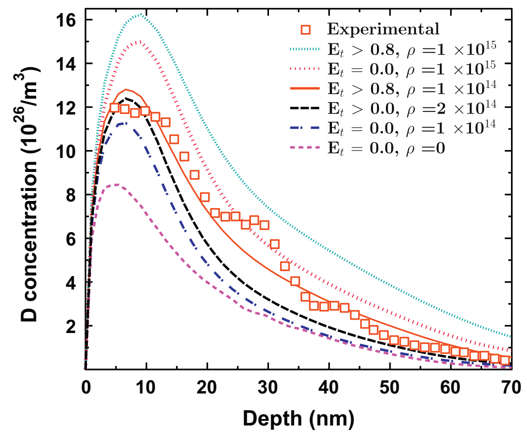

Fig. 3. Simulated 5 keV D profiles with different C-SIA trapping energies: E_t (eV), and dislocation densities: ρ (m^{-2}).

The trapping radius of 0.59 nm for a monovacancy to trap a D atom, was obtained by placing the D atom to varying distances from the monovacancy center, and relaxing each system with the molecular statics method. The W–D potential parameters used for the relaxation was taken from Juslin et al. [41].

The trapping radius of any impurity to trap D was chosen to be the nearest neighbor distance $\sqrt{3}a_0/2 \approx 0.274$ nm.

Table 3
Simulation results. Values are in % compared to the implanted fluence of 5.8×10^{20} D/m^2. Values in parenthesis are % compared to the total amount in the sample.

D implantation energy	5 keV	15 keV	30 keV
Deuterium			
Backscattered during implantation	28.8	17.0	10.2
Diffused to sample surface	63.2	59.0	55.1
Total retained in sample	8.0	23.9	34.7
Trapped in vacancies	(75.3)	(80.7)	(83.1)
Trapped in V_1	(53.9)	(52.7)	(53.7)
Trapped in V_2	(16.3)	(20.4)	(21.9)
Trapped in V_3	(3.8)	(5.0)	(5.0)
Trapped in V_4	(0.9)	(1.9)	(1.9)
Trapped in V_5	(0.5)	(0.7)	(0.5)
Trapped in intrinsic traps[a]	(24.7)	(19.3)	(16.9)
Implantation			
Induced SIA and vacancies	16.3	79.1	155
Interstitials (% of the total induced amount)			
Annihilated	93.0	95.2	96.3
Diffused to surface	1.8	0.5	0.3
Total SIA in sample	5.2	4.4	3.4
In dislocations	2.6	2.3	2.3
In C-SIA$_x$ clusters	2.2	1.9	0.9
In grain boundaries	0.3	0.2	0.3
Vacancies (% of vacancies in each cluster type)			
V_1	71.5	65.3	64.6
V_2	21.7	25.3	26.4
V_3	5.0	6.2	6.1
V_4	1.1	2.3	2.3
V_5	0.7	0.9	0.7

[a] Impurities, grain boundaries and dislocations, see text.

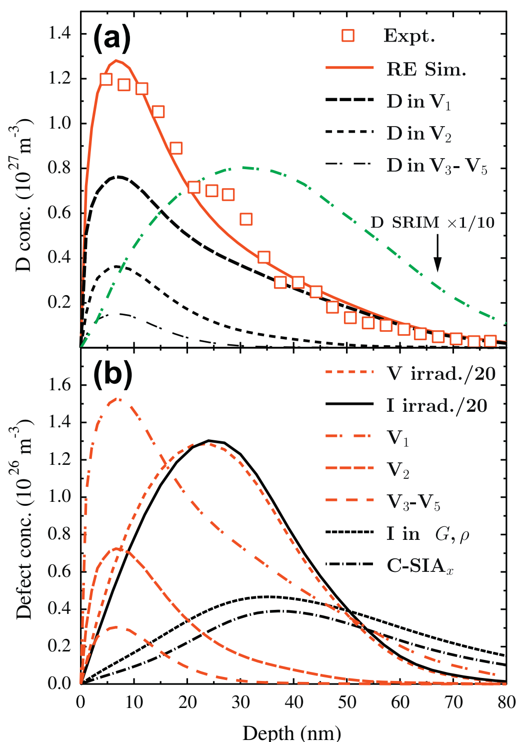

Fig. 4. Details for the 5 keV/D implantation. (a) The total simulated D profile (solid line) consists mainly of D trapped in monovacancies, while the concentration of D trapped in larger vacancy clusters, decreases along with the cluster size. The SRIM simulation, shows the D profile in case where the implantation would have been done at a temperature where D is immobile. (b) Implantation induced and final defect profiles. The remaining (about 5% of the initially produced) SIAs in the sample are in grain boundaries (G), dislocations (ρ) and in carbon impurity SIA$_x$ clusters.

3.4. Detrapping parameters

A fundamental concept to the development of the rate theory, was the formulation of transition state theory [44,45]. The main conclusion of this theory, is that for a bound system to break up, it has to pass a minimum energy barrier called the activation energy.

Entities that can break up are clusters of vacancies, SIAs, and impurity-SIA. D atoms can be detrapped from monovacancies, vacancy clusters, SIA clusters, impurities, dislocations and grain boundaries.

The activation energies for detrapping $E_{A,\delta}$ (often called trapping energy) and attempt frequencies, for one to six D in a monovacancy, was taken from DFT calculations [15]. The trapping energies from a larger vacancy cluster, with m vacancies, are assumed to be the same as for m monovacancies. This approximation works fine with implantation at RT, where mainly trapping occurs. For larger clusters, the binding energy should increase and approach the binding energy of D to the surface.

The D atom is weakly bound to a SIA with a trapping energy of about 0.4 eV [15]. For D trapping to SIA clusters, we tested trapping energies between 0.4 and 1.0 eV, but noticed no significant differences in the RE simulations; the amount of D trapped in vacancies, were always between 100 and 1000 times larger, than in the SIA clusters.

Table 2 summarizes the parameters needed to simulate the D–W system at room temperature.

4. Results and discussion

An excellent agreement between the RE simulated, and all the 5, 15, and 30 keV/D experimental D concentration profiles was found, see Fig. 2. The fraction of the retained D, compared to the implanted fluence of 5.8×10^{20} D/m^2, increases rapidly from about 8% to 35% as the implantation energy increases from 5 to 30 keV/D.

The input parameters used in the RE simulations (Table 2), are taken from other works and the only adjustable parameters were the radius for grains, dislocation density, and trapping energy between SIAs and carbon impurity to form a C-SIA complex.

The best agreement with experiments, was obtained when the dislocation density ρ was about 1×10^{14}/m^2, and the C-SIA trapping energy was >0.8 eV. If the grain radius was >1 µm, its effect was negligible. Grain radius of 5 µm was used in all simulations. The quite large dislocation density of 10^{14}/m^2, is typical for cold-worked W [46], as is the case in this study, where the samples were

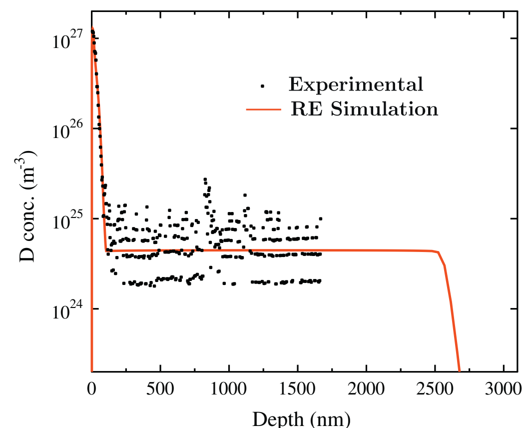

Fig. 5. The experimental and simulated 5 keV/D profiles in logarithmic scale. The simulation was done by adding a D trapping impurity concentration of 4.5×10^{15} cm^{-3}.

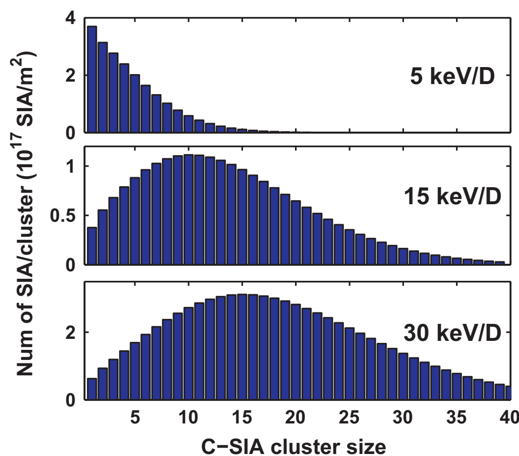

Fig. 6. Number of different sized C-SIA clusters for increasing implantation energy. The mean number of SIAs per cluster is about 5 for 5 keV, 14 for 15 keV and 18 for 30 keV.

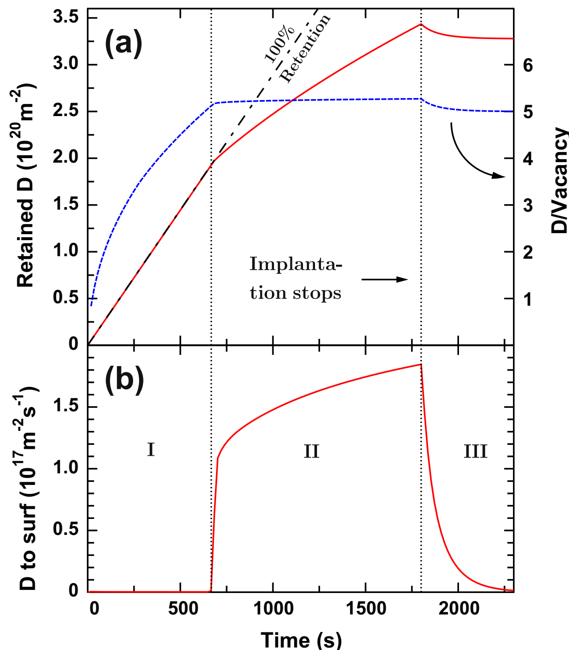

Fig. 7. (a) Retained D and the mean number of D trapped per vacancy, during and after 30 keV/D room temperature implantation. (b) The flux of D atoms from bulk to sample surface. Region I: Vacancies are slowly filling up with D, 100% retention. Region II: Vacancies are saturated with D, and D flux to surface starts. Region III: Weakly bound sixth D detraps from vacancies after the implantation.

mechanically polished without electro-chemical surface removal prior to the D implantation.

It should be emphasized that also other parameter value combinations, give simulation profiles that matches the experimental ones. However, Fig. 3 shows the approximate range of the possible value combinations, in order for the simulations to agree with the experiments. We see that the dislocation density seems to be around 10^{14}/m^2, and that there should be a positive binding energy between a SIA and C atom (bound system, C-SIA). The SIA binding impurity might also be Fe (10 µg/g), Al, Si or O (5 µg/g), or other impurities found in the W material. Experiments with a large concentration of a specific impurity, or DFT simulations are still needed to show which impurities the SIA will be bound to. The consequences of the bound impurity SIA complex is discussed later.

The main reason for the increase in the retained D amount, as SIAs are trapped by C (and/or other impurities) is that then a smaller fraction of the irradiation induced SIAs annihilate with vacancies. Thus, more vacancies that trap D survive, which in turn increases substantially the retained D amount in the sample.

The final simulation outcome after irradiation is presented in Table 3, and for the 5 keV/D case in Fig. 4. The present RE simulation results give not only the total retained D, but quantitative amounts of D trapped in each defect type. Of the total implanted D fluence 5.8×10^{20} D/m^2, at 5 keV about 29% is directly backscattered, 63% diffuse to surface and desorb to vacuum, and only 8% is retained in the sample.

We observe that at 5 keV, about 75% of the retained D is trapped in monovacancies and vacancy clusters, and the rest in impurities, grain boundaries and/or dislocations, extending deep into the sample, see Fig. 5. The maximum range for trapped D, increases from about 2.6 µm at 5 keV, to about 4.5 µm at 30 keV. These deep extending D tails, have also been observed in other experiments, for example by Alimov et al. [47]. At higher fluences, the retained fraction deep in the sample, will eventually be much larger than the fraction close to the surface, which will be especially important for tritium retention. In this study, we can only speculate about the nature of these deep extending traps. They have been observed in both polycrystalline and single crystal material, with the mean trapped D amount being higher in coarse grained, than in single crystal W [47], indicating that part of these D traps could be grain boundaries. The binding of D atoms to grain boundary has been studied by Zhou et al. using DFT [42]. Their result suggests a binding energy between 0.8 and 1.5 eV, which certainly would trap D at room temperature.

The present samples are not coarse grained, and the number of trapping sites at grain boundaries, should not alone be sufficient to account for the experimental value of about 5×10^{24}/m^3. A dislocation density of about 10^{14}/m^2, is also too low to explain the traps. Another additional alternative is, that D is trapped in impurities. One potential trapping impurity present in the sample is oxygen (5 µg/g). Haasz et al. noticed that the D and O depth profiles were quite similar in single crystal W [48]. This finding is a strong indication that O binds D, and DFT calculations are underway to confirm this, and to give a value for the binding energy.

Fig. 4b shows the irradiation induced and the final defect profiles. The irradiation induced profiles, are the sum SIA and vacancy profiles from Fig. 1, times the implanted fluence. The total number of irradiation-induced vacancies and SIAs, per incoming D, is 0.16 at 5 keV, 0.79 at 15 keV, and 1.6 at 30 keV. About 93–96% of these vacancies are annihilated by the diffusing SIAs during the irradiation. The remaining SIAs in the sample have been trapped by dislocations and grain boundaries and C-SIA$_x$ clusters, where x is the number of SIAs in the cluster. The size distributions of the C-SIA$_x$ clusters are shown in Fig. 6, where the total integrated amount of SIAs in these clusters, increase from about 2.1×10^{18}/m^2 for 5 keV, to about 8.1×10^{18}/m^2 for 30 keV implantation. Also, the average cluster size is seen to increase, as more SIAs are produced at higher D implantation energies. These C-SIA$_x$ clusters could be the experimentally observed interstitial type dislocation loops [49].

In this study, the flux of D, and the corresponding SIA production rate, is too small for producing large SIA or D-SIA clusters. Large SIA clusters were only observed, if we assumed that there is an impurity that initially forms a bound complex with a SIA. This complex then serves as a nucleation site for large impurity-SIA clusters. If the SIA production rate would be large enough, large SIA clusters could form without the need of impurities. Further evidence for the formation of impurity-SIA complexes, is given by the 8 keV H irradiation experiment by Sakamoto et al. [50], showing

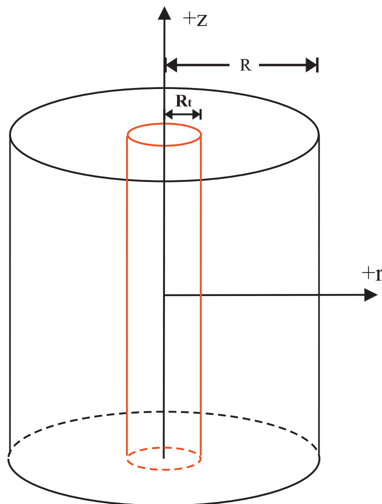

Fig. A.1. Cylindrical cell to derive sink strength for edge dislocations.

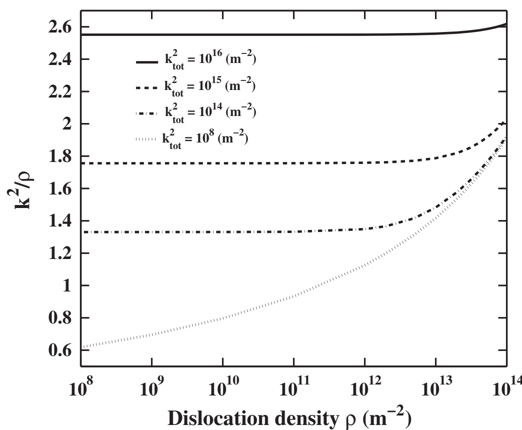

Fig. A.2. Sink strength for dislocations divided by dislocation density ρ for increasing total sink strengths. The usual approximation that the sink strength for dislocations is about ρ at low dislocation density and no other sinks present holds.

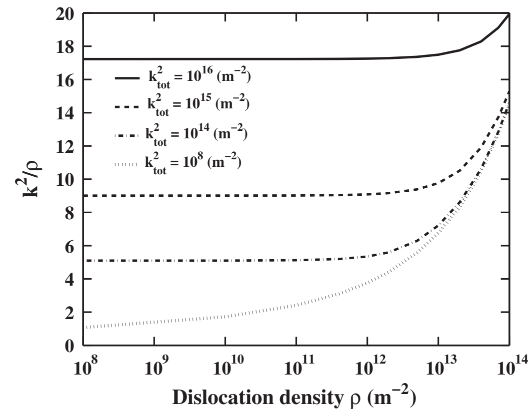

Fig. A.3. Sink strength for dislocations divided by dislocation density ρ for increasing total sink strengths including SIA-dislocation interactions.

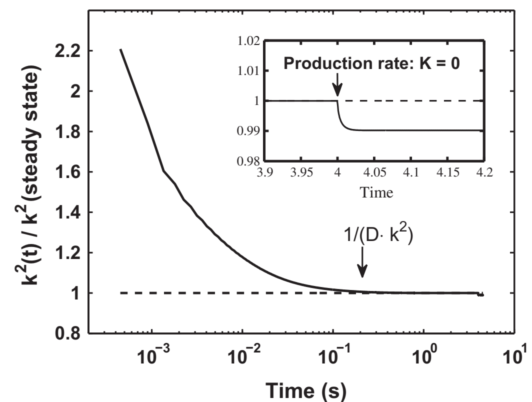

Fig. A.4. Time dependence for the numerical sink strength.

that the interstitial dislocation loop areal density increases when the impurity concentration increases.

A remarkable observation is that the final retained D profile, Fig. 4a, does not resemble neither the implanted D, nor the irradiation induced vacancy profile Fig. 4b. During the D induced collision cascades, the vacancies are produced on average, a bit closer to the surface than the SIAs. The SIA-vacancy annihilation is proportional to both their respective concentrations, resulting in that vacancies deeper than about 30 nm, are effectively annihilated, and therefore, the remaining vacancy profile is shifted towards the surface. Hence, any short time and D fluence simulation method trying to produce the observed retained D profile will fail, because the vacancy, and in the vacancies trapped D profiles will shift more and more towards the surface with increasing D fluence.

Next in Fig. 7a is visualized the time evolution of the retained D during, and shortly after the 30 keV/D room temperature implantation. In the figure, three distinct regions are elucidated. In region I, the retained D is the same as the implanted one (100% retention, backscattered fraction excluded).

In region II, the vacancies become saturated with D, and the mean number of trapped D per vacancy, is between five and six. All the implanted D atoms are no longer trapped, but diffuse deeper into the sample, and to the sample surface. In Fig. 7b is shown the simultaneous onset of D atom flux to the W surface. After the implantation has stopped (region III), the D retention drops and a remnant D flux to the W surface takes place for about 10 min. The simulation results show that the slow decrease in the retained D, is the detrapping of the sixth D from monovacancies (trapping energy 0.61 eV, Table 2). This post implantation effect has been seen experimentally for example by García-Rosales et al. [3] and Pisarev et al. [7] where the observed D_2 desorption from the sample surface, resembles the present simulated D flux to surface in Fig. 7b.

5. Conclusions

The simulation capabilities using rate theory equations, were extended to include also the dynamic processes during particle irradiation. These improvements have at least the following advantages. Firstly, there is no need to assume any H trapping defect profiles, because they evolve naturally during the simulations. Secondly, the simulation results give H trapped in each defect type, not only the total retained amount. However, solving the large number of coupled differential equations, need a lot of computer power.

The simulation results were seen to be in excellent agreement with experiments, where each monovacancy or vacancy cluster contains about five H per vacancy. Only a small amount of H is trapped in SIA clusters.

The observed H traps deep in the sample, that will be decisive to T retention in fusion machines like ITER, are probably grain

boundaries, dislocations and impurities. One likely impurity candidate that traps H seems to be oxygen, but confirmation is still needed.

Impurities were seen to trap SIAs, which then act as nucleation sites for formation of large interstitial clusters. An obvious interpretation is that the formed clusters are the interstitial type dislocation loops observed experimentally.

Acknowledgments

The research was supported by Association EURATOM-TEKES under the FUSION program. Grants of computer time from the Center for Scientific Computing (CSC) in Espoo, Finland are gratefully acknowledged.

Appendix A. The sink strength of edge dislocations

To derive the sink strength for dislocations, we must begin by defining the sink strength and how it follows from the continuity equation. The actual proof to this theory is given by Brailsford and Bullough [37]. Consider a material where impurities, point and extended defects are randomly distributed and we can describe each entity type, called hereafter defect, with its own concentration profile extending in three dimensions $c = f(x, y, z)$. The defect concentration profile [m^{-3}] must obey the continuity equation

$$\frac{\partial c}{\partial t} + \vec{\nabla} \cdot \overrightarrow{F} = K \tag{A.1}$$

where $\vec{F}$ is the flux vector $D\frac{d\overrightarrow{C}}{dr}$ of defects per unit area and time [$m^{-2}\, s^{-1}$] entering and leaving the system, $\vec{\nabla} \cdot \overrightarrow{F}$ is the divergence of each flux and K is the defect production rate per volume per second [$m^{-3}\, s^{-1}$]. We choose a cell volume V and integrate the continuity equation over this volume to get

$$\int_{V_m} \frac{\partial c}{\partial t} dV + \int_{V_m} (\vec{\nabla} \cdot \vec{F}) dV = KV_m, \tag{A.2}$$

where V_m is the so called matrix volume which is the total cell volume minus all sink volumes (defect concentration is zero inside the sinks). The cell volume is chosen to be large enough to include the same number of each sink type as cells bounding to this volume. Therefore the net flux of defects between identical cells is zero and only sinks need to be included in the surface integrals

$$\int_{V_m} \frac{\partial c}{\partial t} dV + \sum_i \int_{V_m} (N_i \vec{\nabla} \cdot \vec{F_i}) dV = KV_m, \tag{A.3}$$

where N_i is the number of each different sink type i and $\vec{F_i}$ is the flux of defects entering all sinks in this system. No reemission of defects from sinks is considered here. This transforms with the help of the divergens theorem

$$\int_V (\vec{\nabla} \cdot \overrightarrow{A}) dV = \int_S (\overrightarrow{A} \cdot \vec{n}) dS, \tag{A.4}$$

to

$$\int_{V_m} \frac{\partial c}{\partial t} dV + \sum_i N_i \int_{S_i} (\overrightarrow{F_i} \cdot \vec{n}) dS = KV_m. \tag{A.5}$$

If further the volume is constant in time, or dV_m/dt is small, we can write Eq. (A.5) as

$$\frac{d}{dt}\left(\int_{V_m} c dV\right) = -\sum_i N_i \int_{S_i} (\overrightarrow{F_i} \cdot \vec{n}) dS + KV_m.$$

We divide this by the total volume and identify $\left(\frac{\int_{V_m} c dV}{V}\right)$ as the mean concentration of defects in the volume denoted by $\langle c \rangle$ and get

$$\frac{d\langle c \rangle}{dt} = -\sum_i \frac{N_i}{V} \int_{S_i} (\overrightarrow{F_i} \cdot \vec{n}) dS + K\frac{V_m}{V}. \tag{A.6}$$

The flux of defects to each sink should be proportional to the mean defect concentration and diffusion coefficient for the defect. This brings us to the following definition for each sink type

$$\frac{N_i}{V} \int_{S_i} (\overrightarrow{F_i} \cdot \vec{n}) dS = k_i^2 D \langle c \rangle \tag{A.7}$$

which defines the sink strength for sink type i as

$$k_i^2 = \frac{\frac{N_i}{V} \int_{S_i} (\overrightarrow{F_i} \cdot \vec{n}) dS}{D\langle c \rangle}. \tag{A.8}$$

The sink strength is proportional to the sink concentration and sink surface area and inversely proportional to the defect diffusion coefficient and mean concentration. To realize how complicated parameter the sink strength is we insert Eq. (A.7) in Eq. (A.6) to obtain

$$\frac{d\langle c \rangle}{dt} = -\left(\sum_i k_i^2\right) D\langle c \rangle + K\frac{V_m}{V}. \tag{A.9}$$

The steady state solution ($d\langle c \rangle/dt = 0$) gives

$$\langle c \rangle = \frac{K\frac{V_m}{V}}{\left(\sum_i k_i^2\right) D}, \tag{A.10}$$

which, when compared to Eq. (A.8), clearly shows that each sink strength also depends on all the sink strengths for some specific defect like for example the SIA.

If the sink is symmetric and the flux of defects to the sink boundary is constant from all directions $|\overrightarrow{F}_i| = \text{constant}$, we can write the surface integral, Eq. (A.8), for this sink simply as

$$\int_{S_i} (\overrightarrow{F_i} \cdot \vec{n}) dS = |F_i| S_i, \tag{A.11}$$

where S_i is the surface area. The sink strength is thus

$$k_i^2 = \frac{\frac{N_i}{V} (|F_i| S_i)}{D\langle c \rangle}. \tag{A.12}$$

Now we derive the sink strength of line absorbers, i.e. edge dislocations. We first neglect the dislocation-defect interaction and define a cylindrically symmetrical cell with radius R with an edge dislocation with trapping radius R_t with its center along z-axis, see Fig. A.1. (See Fig. A.2)

All the sinks are randomly distributed in the cell. The cell should be large enough so that we could choose any other sink as origin without changing the mean number of any sink type in the cell. At time $t = 0$ the defects starts to be produced in the whole volume with production rate K [$m^{-3}\, s^{-1}$]. A cylindrically symmetrical defect concentration profile as a function of r from the origin and time t develops. The defect diffuses with diffusion coefficient D. This profile satisfies following equation with other sinks with sum sink strength $k_{tot}^2 = \sum_i k_i^2$ (including the sink strength for other edge dislocations)

$$\frac{dc}{dt} = D\nabla^2 c - Dk_{tot}^2 (c - c_{eq}) + K \tag{A.13}$$

where c_{eq} is the equilibrium concentration of the defect. The differential equation in the cell reads in cylindrical coordinates

$$\frac{\partial c}{\partial t} = D\left[\frac{\partial^2 c}{\partial r^2} + \frac{1}{r}\frac{\partial c}{\partial r} - k_{tot}^2 (c - c_{eq})\right] + K. \tag{A.14}$$

The steady state solution ($\partial c/\partial t = 0$) of Eq. (A.14) with $c_{eq} = 0$ yields

$$c(r) = \frac{K}{Dk_{tot}^2 P}[P - (I_1(k_{tot}R)K_0(k_{tot}r) + K_1(k_{tot}R)I_0(k_{tot}r))] \quad (A.15)$$

where $P = I_0(k_{tot}R_t)K_1(k_{tot}R) + K_0(k_{tot}R_t)I_1(k_{tot}R)$, and I_v and K_v are the modified Bessel function of first and second kind, respectively. The inward steady state flux of defects at the dislocation matrix edge is

$$|F| = D\frac{\partial c}{\partial r}\bigg|_{r=R_t} = \frac{K}{k_{tot}P}[I_1(k_{tot}R)K_1(k_{tot}R_t) - K_1(k_{tot}R)I_1(k_{tot}R_t)]$$

The mean defect concentration in the cylinder is ($c_{eq} = 0$)

$$\langle c \rangle = \frac{K}{Dk_{tot}^2}\left[1 - \frac{Rt^2}{R^2} + \frac{2R_t}{R^2 k_{tot}P}(I_1(k_{tot}R_t)K_1(k_{tot}R) - I_1(k_{tot}R)K_1(k_{tot}R_t))\right]. \quad (A.16)$$

The sink strength from Eq. (A.12) becomes as a function of the dislocation areal density $\rho = 1/(\pi R^2)$, and parameters $Q = \frac{k_{tot}}{\sqrt{\pi\rho}}$ and $S = k_{tot}R_t$

$$k^2 = \frac{\rho 2\pi R_t k_{tot}[I_1(Q)K_1(S) - K_1(Q)I_1(S)]}{[P(1 - \pi\rho Rt^2) + \frac{2\pi\rho R_t}{k_{tot}}(I_1(S)K_1(Q) - I_1(Q)K_1(S))]}$$

In reality, dislocation and defect interact through the strain field and when determining sinks strengths, the dislocation-defect interaction has to be taken into account. This can be done by adding a drift term to Eq. (A.13) [51]

$$\frac{dc}{dt} = D\left(\nabla^2 c + \frac{\nabla c \nabla E + c\nabla^2 E}{k_B T}\right) - \left(\sum_i k_i^2\right)Dc + K$$
$$= D\frac{\partial^2 c}{\partial r^2} + \frac{\partial c}{\partial r}\left(\frac{D}{r} + D\frac{\nabla E}{k_B T}\right) + c\left(D\frac{\nabla^2 E}{k_B T} - D\left(\sum_i k_i^2\right)\right) + K \quad (A.17)$$

where the stress effects on the diffusion coefficient has been neglected and the dislocation-defect interaction energy E is assumed to have cylindrical symmetry [52]

$$\frac{E}{k_B T} = -L\left(\frac{1}{r} + \frac{1}{2R - r}\right) \quad (A.18)$$

where the amplitude term L is proportional to the relaxation volume of the defect $|V^r|\Omega$

$$L = \frac{\mu|b|(1+\nu)|V^r|\Omega}{3\pi(1-\nu)k_B T}. \quad (A.19)$$

μ is the shear modulus, $|b|$ the magnitude of the burgers vector for the dislocation and ν is the Poisson's ratio. Eq. (A.17) was solved numerically. The numerical solution for dislocation sink strength with W material and SIA parameters: $\mu \approx 161$ GPa, $|b| \approx a/\sqrt{2} \approx 0.224$ nm, $\nu \approx 0.28$, $R_t = 1$ nm and $|V^r|\Omega = 1.6\,\Omega$ [36], is given in Fig. A.3. We can observe that including SIA-dislocation interactions increases the sink strength noticeably. Because the interaction is proportional to the defect relaxation volume, there is a bias in SIA elimination to dislocations compared to vacancies. The numerically solved dislocation sink strengths were used for SIAs and SIA clusters in the present RE simulations.

One important issue remaining is that the sink strengths used in this study, and generally in the studies found in the literature, are derived assuming steady state conditions Eq. (A.10). However, as pointed out by Rauh et al. [53], the steady state sink strength underestimates the correct sink strength during the initial stages of the irradiation. To check the influence of this to the present study, we solved Eq. (A.17) as a function of time. The production rate K was constant for four seconds, after which it dropped to zero. The obtained dynamic sink strength divided by the steady state sink strength is plotted in Fig. A.4 as a function of time. It can be seen that the dynamic sink strength is initially larger, but rapidly approaches the steady state sink strength (x-axis in log scale). The approximate time scale when the actual sink strength has attained the steady state value is about $1/(Dk^2)$. The conclusion is that the slower the defect diffusion coefficient is and the smaller the total sink strength for that defect to be trapped in sinks is, the longer is the time before the actual dynamic sink strength attains the steady state value. The slowest entity needed to be considered in this study is D with a diffusion coefficient of 1.5×10^{-12} m^2/s, Table 2. Consequently, even with a small total sink strength of about 10^{-14} m^{-2}, steady state is achieved in milliseconds. The total irradiation time of about 1800 s is surely long enough that no dynamic sink strengths are needed in this study. Finally, it is worth mentioning that the proper steady state sink strengths are obtained only assuming a homogeneous defect production and defect concentration in three dimensional space. The present irradiation source term is homogeneous in the sample surface plane (in two dimensions) but varies with depth, Fig. 1. Therefore, the calculated sink strengths might be different from the actual sink strengths at least where the concentration profiles are changing noticeably with depth. The depth dependent sink strengths are however, not considered further in this study.

References

[1] ITER Physics Basis Editors, ITER physics expert group chairs and co-chairs and iter joint central team and physics integration unit, Iter physics basis, Nucl. Fus. 39 (1999) 2137.
[2] A.T. Peacock, Overview of recent european materials r& d activities related to iter, J. Nucl. Mater. 329–333 (2004) 173.
[3] C. García-Rosales, P. Franzen, H. Plank, J. Roth, E. Gauthier, J. Nucl. Mater. 233–237 (1996) 803.
[4] R. Causey, K. Wilson, T. Venhaus, W.R. Wampler, J. Nucl. Mater. 266–269 (1999) 467.
[5] T. Venhaus, R. Causey, R. Doerner, T. Abeln, J. Nucl. Mater. 290–293 (2001) 505.
[6] B. Oliver, T. Venhaus, R. Causey, F. Garner, S. Maloy, J. Nucl. Mater. 307–311 (2002) 1418.
[7] A.A. Pisarev, I.D. Voskresensky, S.I. Porfirev, J. Nucl. Mater. 313–316 (2003) 604.
[8] M. Poon, A. Haasz, J. Davis, J. Nucl. Mater. 374 (2008) 390.
[9] P. Wienhold, M. Profant, F. Waelbroeck, J. Winter, J. Nucl. Mater. 93–94 (1980) 866.
[10] M.I. Baskes, Sandia National Laboratories, Preprint SAND 83-8231.
[11] G. Gervasini, F. Reiter, J. Nucl. Mater. 212–215 (1994) 1379.
[12] G.R. Longhurst, TMAP7: Tritium Migration Analysis Program, User Manual, Idaho National Laboratory, INEEL/EXT-04-02352, 2004.
[13] P.M. Derlet, D. Nguyen-Manh, S.L. Dudarev, Phys. Rev. B 76 (2007) 054107.
[14] D. Nguyen-Manh, A.P. Horsfield, S.L. Dudarev, Phys. Rev. B 73 (2006) 020101.
[15] K. Heinola, T. Ahlgren, K. Nordlund, J. Keinonen, Phys. Rev. B 82 (2010) 094102.
[16] K. Heinola, T. Ahlgren, E. Vainonen-Ahlgren, J. Likonen, J. Keinonen, Physica Scripta T128 (2007) 91.
[17] A. McNabb, P.K. Foster, Trans. Metal. Soc. AIME 227 (1963) 618.
[18] M.I. Baskes, W.D. Wilson, Phys. Rev. B 27 (1983) 2210.
[19] S.M. Myers, P. Nordlander, F. Besenbacher, J.K. Nørskov, Phil. Mag. A 48 (1983) 397.
[20] C. Wert, C. Zener, J. Appl. Phys. 21 (1949) 5.
[21] F.S. Ham, J. Phys. Chem. Solids 6 (1958) 335.
[22] A. Brailsford, R. Bullough, J. Nucl. Mater. 44 (1972) 121.
[23] S. Arrhenius, Z. Phys. Chem. (Leipzig) 4 (1889) 226.
[24] J.A. Christiansen, H.A. Kramers, Z. Phys. Chem. (Leipzig) 104 (1923) 45.
[25] H. Eyring, M. Polanyi, Z. Phys. Chem. B 12 (1931) 19.
[26] E. Pollak, P. Talkner, Chaos 15 (2005) 026116.
[27] K. Heinola, T. Ahlgren, Phys. Rev. B 81 (2010) 073409.
[28] E. Vainonen-Ahlgren, T. Ahlgren, J. Likonen, S. Lehto, T. Sajavaara, W. Rydman, J. Keinonen, C.H. Wu, Phys. Rev. B 63 (2001) 045406.
[29] Y.-L. Liu, H.-B. Zhou, S. Jin, Y. Zhang, G.-H. Lu, J. Phys.: Condens. Matter 22 (2010) 445504.
[30] K.-D. Rasch, R.W. Siegel, H. Schultz, Phil. Mag. A 41 (1980) 91.
[31] B.D. Wirth, G.R. Odette, D. Maroudas, G. Lucas, J. Nucl. Mater. 244 (1997) 185.
[32] Y.N. Osetsky, D.J. Bacon, A. Serra, B.N. Singh, S.I. Golubov, J. Nucl. Mater. 276 (2000) 65.
[33] N. Soneda, T. Diaz de la Rubia, Philos. Mag. A 81 (2001) 331.
[34] J.F. Ziegler, SRIM-2011 Software Package. <http://www.srim.org>.
[35] K. Nordlund, Comput. Mater. Sci. 3 (1995) 448.
[36] T. Ahlgren, K. Heinola, N. Juslin, A. Kuronen, J. Appl. Phys. 107 (2010) 033516.
[37] A.D. Brailsford, R. Bullough, Philos. Trans. R. Soc. Lond. 302 (1981) 87.
[38] L. Malerba, C.S. Becquart, C. Domain, J. Nucl. Mater. 360 (2007) 159.
[39] A.V. Barashev, S.I. Golubov, H. Trinkaus, Philos. Mag. A 81 (2001) 2515.
[40] H. Trinkaus, H.L. Heinisch, A.V. Barashev, S.I. Golubov, B.N. Singh, Phys. Rev. B 66 (2002) 060105.
[41] N. Juslin, P. Erhart, P. Träskelin, J. Nord, K.O.E. Henriksson, E. Salonen, K. Nordlund, K. Albe, J. Appl. Phys. 98 (2005) 123520.

[42] H.-B. Zhou, Y.-L. Liu, S. Jin, Y. Zhang, Nucl. Fus. 50 (2010) 025016.
[43] C. Becquart, C. Domain, U. Sarkar, A. DeBacker, M. Hou, J. Nucl. Mater. 403 (2010) 75.
[44] E. Wigner, Z. Phys. Chem. Abt. 19 (1932) 203.
[45] H. Eyring, J. Chem. Phys. 3 (1935) 107.
[46] E. Lassner, W.-D. Schubert, Tungsten, Properties, Chemistry, Technology of the Element, Alloys, and Chemical Compounds, Cluwer Academic, Plenum Publishers, New York, 1999.
[47] V.K. Alimov, J. Roth, R. Causey, D. Komarov, C. Linsmeier, A. Wiltner, F. Kost, S. Lindig, J. Nucl. Mater. 375 (2008) 192.
[48] A. Haasz, M. Poon, R. Macaulay-Newcombe, J. Davis, J. Nucl. Mater. 290–293 (2001) 85.
[49] T. Matsui, S. Muto, T. Tanabe, J. Nucl. Mater. 283–287 (2000) 1139.
[50] R. Sakamoto, T. Muroga, N. Yoshida, J. Nucl. Mater. 220–222 (1995) 819.
[51] P.G. Shewmon, Diffusion in Solids, The Minerals, Metals & Materials Society, Pennsylvania, 1989.
[52] R.J. White, S.B. Fisher, P.T. Heald, Philos. Mag. 34 (1976) 647.
[53] H. Rauh, R. Bullough, M.H. Wood, Proc. R. Soc. Lond. A 388 (1983) 311.